Phase-Field Modeling of Fracture for Heterogeneous Materials and Shell Structures

Van-Hoi Nguyen(웬반호이) [1], Minh-Chien Trinh(트린민첸) [2], Hyungmin Jun(전형민) [1,2,*]
School of Mechanical-Aerospace-Electric Convergence Engineering [1], Department of Mechanical Systems Engineering [2]
*hjun@jbnu.edu

Topic #1 Thermal Damage of FGMs

Extended phase-field models with high accuracy are developed to investigate thermal-induced fracture in functionally graded composites.

The proposed models are validated against experimental results, demonstrating excellent agreement in fracture behavior.

The temporal evolution of strain energy, fracture energy, and stress distribution during crack propagation is comprehensively examined.

Phase-field Modeling of Thermal Fracture

Diffuse crack

- Boundary conditions

$$\begin{cases} \nabla d \cdot \mathbf{n} = 0, & \text{on } \partial\Omega, \\ \boldsymbol{\sigma}_{el} \cdot \mathbf{n} = \bar{\mathbf{t}}, & \text{on } \partial\Omega_t, \\ \mathbf{J} \cdot \mathbf{n} = \bar{\mathbf{J}}, & \text{on } \partial\Omega_J. \end{cases}$$

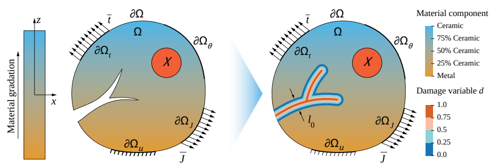

- Governing equations

$$\begin{cases} \rho \ddot{\mathbf{u}} = \nabla \cdot \boldsymbol{\sigma}_{el} + \mathbf{b}, & \text{in } \Omega, \\ \rho(z) c_p(z) \dot{\theta} + \nabla \cdot \mathbf{J} = \chi, & \text{in } \Omega, \\ \frac{G_c(z)}{4 l_0} d - G_c(z) l_0 \nabla \cdot \nabla d = (1-d) H_+, & \text{in } \Omega. \end{cases}$$

- Rule of mixtures

$$P(z) = P_m V_m + P_c V_c$$

- Energy release rate for material components

$$G_c^m = \frac{256}{27}\frac{(\sigma_f^m)^2 l_0}{E} \text{ and } G_c^c = \frac{256}{27}\frac{(\sigma_f^c)^2 l_0}{E}$$

Numerical Examples of Crack Propagation

Crack propagation in bi-material plates [1]

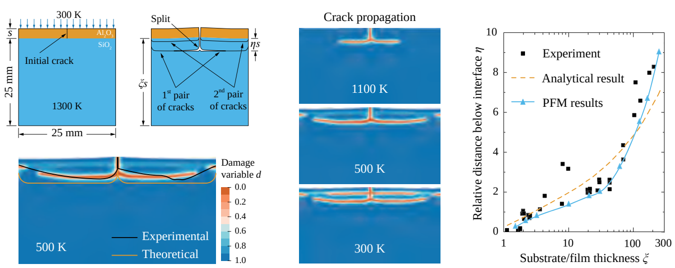

Burner heating test of functionally graded coating plates

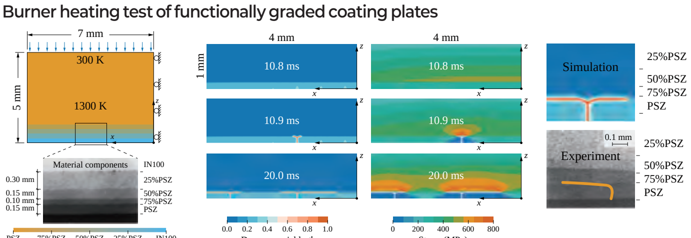

» The proposed model of thermal fracture in FGMs demonstrates excellent agreement with experimental results in both examples compared to the theoretical model.

Circular Functionally Graded Material Plate

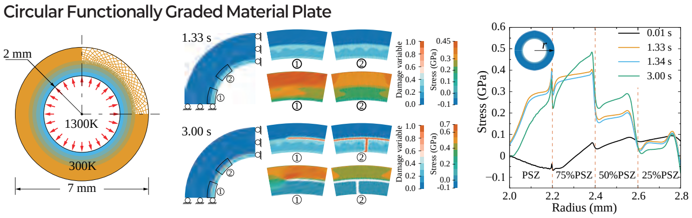

Circular plate | Temporal damage and stress fields | Thermal mismatch stress

» The thermal mismatch at the interfaces between the PSZ and 75 %PSZ layers can increase the stress in the PSZ layer by 30 % and reduce the stress in the 75 %PSZ layer by 20 %.

Topic #2 Dynamic Ductile Fracture in Shells

A phase-field formulation incorporating general curved shell kinematics is firstly developed to model dynamic ductile fracture.

A refined alternate minimization scheme is introduced to efficiently simulate large-deformation fracture processes.

The approach is validated through numerical reproduction of dynamic fracture experiments, demonstrating accurate prediction of complex failure patterns.

General Curved Shell Finite Element with Diffuse Cracks

Diffuse crack

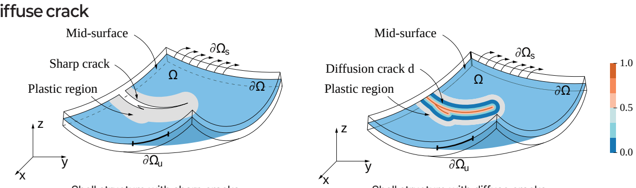

- Free energy:

$$\mathcal{E} = \int_{{}^t\Omega} \left(g(d,c)\psi_e^+ + \psi_e^- + \psi_p + \psi_h + \psi_{frac} \right) dV + \int_{{}^t\Omega} b_i u_i \, dV + \int_{\partial^t\Omega_t} t_i u_i \, dS \quad \text{where} \quad g(d,c) = (1-d)^{2c} + \eta$$

General curved shell kinematics

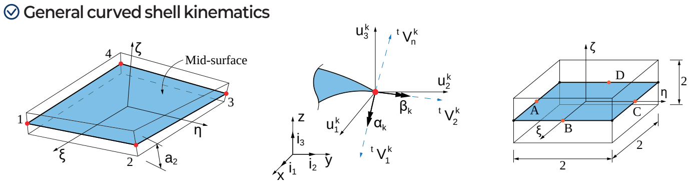

- Incremental displacement field:

$$_0\mathbf{u}(\xi,\eta,\zeta) = \sum_{k=1}^{4} h_k(\xi,\eta)\, {}_0\mathbf{u}^k + \frac{\zeta}{2}\sum_{k=1}^{4} a_k h_k(\xi,\eta)\left({}^{t+\Delta t}\mathbf{V}_n^k - {}^t\mathbf{V}_n^k\right)$$

Linearized equilibrium equations

$$\int_{\Omega_0} \rho\, {}^{t+\Delta t}\ddot{u}_i \delta_0 u_i \, dV + \int_{\Omega_0} {}_0S_{ij} \delta_0 E_{ij}^L \, dV + \int_{\Omega_0} {}^t_0S_{ij} \delta_0 E_{ij}^{NL} \, dV = {}^{t+\Delta t}\mathcal{R} - \int_{\Omega_0} \rho\, {}^t_0\ddot{u}_i \delta_0 u_i \, dV - \int_{\Omega_0} {}^t_0S_{ij} \delta_0 E_{ij}^L \, dV$$

$$\int_{\Omega_0} \left(g_{,dd}({}^t d, p)\frac{\mathcal{H}^*}{G_c} + \frac{1}{l_0} \right)_0 d\, \delta_0 d \, dV + \int_{\Omega_0} l_0\, {}_0d_{,i} \delta_0 d_{,i} \, dV = -\int_{\Omega_0} \left(g_{,d}({}^t d, p)\frac{\mathcal{H}^*}{G_c} + \frac{1}{l_0} \right) \delta_0 d \, dV - \int_{\Omega_0} l_0\, {}^t d_{,i} \delta_0 d_{,i} \, dV$$

In-house Codes Verification with Benchmark Test Problems

Out-of-plane stretching and tearing fracture test [4]

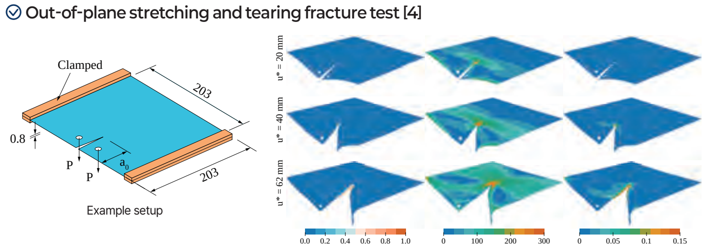

Circular steel plate subjected to an underwater blast load

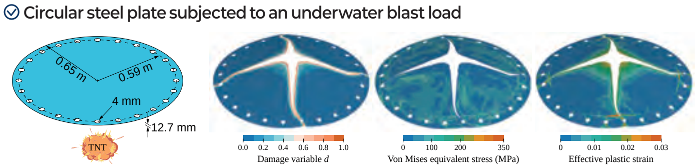

Example setup | Simulation results after 5 ms

» The proposed ductile fracture model exhibits excellent agreement with experimental observations, achieving superior accuracy compared to the existing model [3].

Acknowledgments & References

[1] Nguyen, V.H., Trinh, M.C. & Jun, H. (2024). Fracture behavior of thermal mismatch in functionally graded materials using phase-field modeling. Engineering Fracture Mechanics, 310:110433.
[2] Trinh, M.C. & Jun, H. (2021). A higher-order quadrilateral shell finite element for geometrically nonlinear analysis. European Journal of Mechanics / A Solids, 89: 104283.
[3] Trinh, M.C. & Jun, H. (2023). Geometrically nonlinear analysis of functionally graded composite shells using MITC4 and MITC9 elements. Thin-Walled Structures, 185: 110632.
[4] Nguyen, V.H., Trinh, M.C. & Jun, H. (2025). A phase-field modeling of dynamic ductile fracture in general shell structures, In preparation.

NRF 한국연구재단 KIAT 한국산업기술진흥원 IPET 농림식품기술기획평가원 KHIDI 한국보건산업진흥원 BK21 FOUR

Computational Mechanics

Comprehensive Study of Spectral Thermoelastic Stability in Structural Multimaterial Topology Optimization

Thanh T. Banh(탄반티엔) [1], Minh-Chien Trinh(트린민첸) [2], Hyungmin Jun(전형민) [1,2,*]
School of Mechanical-Aerospace-Electric Convergence Engineering [1], Department of Mechanical Systems Engineering [2]
*hjun@jbnu.edu

Topic #1 / Thermoelastic Vibration Stability

This study proposes a stability-preserving load regulation (SPLR) scheme to address the limitations of existing approaches in capturing thermoelastic vibration behavior of coupled systems.

It further extends the framework to frequency-based problems that cannot be reliably solved without consistent consideration of both eigenfrequency and thermal stability effects in coupled systems.

It comprehensively broadens the applicability of the method to encompass multimaterial configurations and fully 3D modeling.

Generalized SIMP-based Multimaterial Model

- Generalized Solid Isotropic Material with Penalization (Generalized SIMP)

$$\mathcal{F}^{e,\mathrm{int}}(\alpha_1,\alpha_2) = (\alpha_1)^{p_1}(\alpha_2)^{p_2}\mathcal{F}^{e,1} + (\alpha_1)^{p_1}[1-(\alpha_2)^{p_2}]\mathcal{F}^{e,2} + \varepsilon_c[1-(\alpha_1)^{p_1}]\mathcal{F}^{e,s}$$

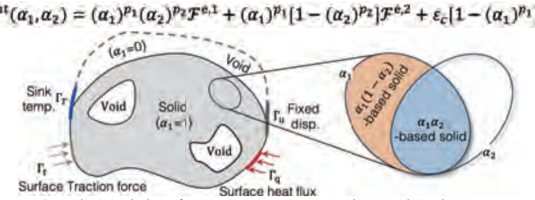

Graphical depiction of a coupled thermomechanical multiphysics system

SPLR for Thermoelastic Free Vibration

- Aims to keeps the vibrating system pre-buckling

$$(\mathbf{K} + \varrho^{\mathrm{splr}}\mathbf{K}^{\mathrm{t}})\mathbf{q}^{\alpha} = \omega_\alpha^2\mathbf{M}\mathbf{q}^{\alpha}.$$

(+) Necessary conditions:

$$\varrho^{\mathrm{splr}} = \varrho^{\mathrm{splr}}(\varrho_{\mathrm{cr}}) = \begin{cases}(1-\zeta)\varrho_{\mathrm{cr}} & \text{if } \varrho_{\mathrm{cr}} \le 1,\\ 1 & \text{if } \varrho_{\mathrm{cr}} > 1,\end{cases}$$

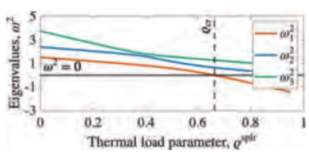

(+) Sufficient conditions: $\varrho_{\mathrm{cr}} = \varrho_1 > 1$ with ϱ_{cr} is critical BLF of $\det(\mathbf{K} + \varrho\mathbf{K}^{\mathrm{t}}) = 0$.

- Remark: Final loop satisfies $\omega_1 = \omega_{0,1}$ ($\omega_{0,1}$ from $\det[(\mathbf{K}+\mathbf{K}^{\mathrm{t}}) - \omega_0\mathbf{M}] = 0$).

Numerical Examples

- Thermal Compliance Optimization of a 2D Beam

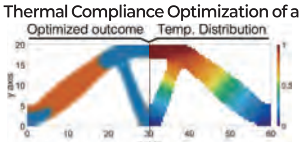

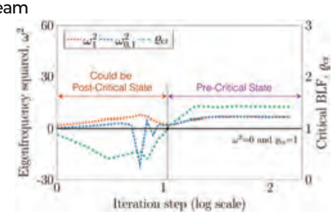

Optimized 2D beam ($C = 9.0, \varrho_{cr} = 1.4, \omega_1 = \omega_{0,1}$)

- As observed, $\varrho_{cr} < 1$ during several iterations, leading to $\omega_{0,1}^2 < 0$. In contrast, $\omega_1^2 > 0$ throughout the process, and $\omega_1 = \omega_{0,1}$ at the final iteration.

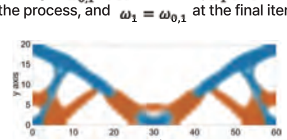

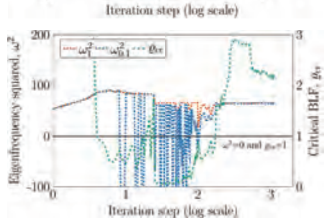

Optimized outcome under $\omega_{0,1} \ge 8.0$ ($C = 14.6, \varrho_{cr} = 2.0, \omega_1 = \omega_{0,1} = 8.0$)

- All $\omega_1^2 > 0$ during the process, leading the optimized $\omega_{0,1}^2$ also converges to a positive value.

- Fundamental Frequency Optimization for 3D plate

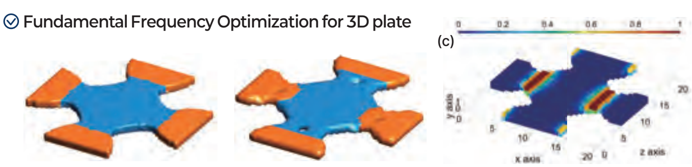

Optimized 3D plates: (a) no thermal effect, (b) with two heat sources; (c) temperature field of (b).

Topic #2 / Thermoelastic Buckling Stability

A comprehensive framework is established for structural stability, enabling consistent integration of thermoelastic buckling shell analysis.

A novel SPLR is proposed to maintain spectral consistency and numerical stability, eliminating complex-valued decoupled buckling load factors and ensuring reliable stability evaluation throughout the process.

The refined adaptive continuum method (RACM) is extended to coupled multiphysics systems, and a refined stabilization technique is introduced to suppress artificial buckling modes.

Shell Geometry and Field Interpolations

- A mapping from (r,s,t) to (x,y,z):

$$\vec{x} = \sum_{i=1}^{4}\chi_i(r,s)\left(\vec{x}_i + t\frac{a_i}{2}\vec{V}^{3i}\right).$$

- Displacement field:

$$\vec{u}\big|_{\Omega^e} = \sum_{i=1}^{4}\chi_i\left[\vec{u}_i + t\frac{a_i}{2}(-\beta_i^1\vec{V}^{2i} + \beta_i^2\vec{V}^{1i})\right].$$

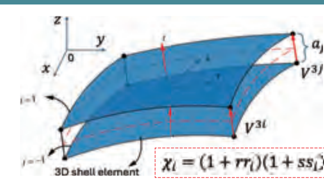

- Temperature field:

$$T\big|_{\Omega^e} = \sum_{i=1}^{4}\left[\chi_i(r,s)\frac{1-t}{2} \quad \chi_i(r,s)\frac{1+t}{2}\right]\begin{Bmatrix}T_i^{\mathrm{bot}}\\ T_i^{\mathrm{top}}\end{Bmatrix} = \sum_{i=1}^{8}\tau_iT_i = \boldsymbol{\tau}\mathbf{T}^e.$$

SPLR and RACM for Thermoelastic Buckling

- Aims to keep the baseline term in the following surrogate model positive definite:

$$[(\mathbf{K} + \varrho^{\mathrm{splr}}\mathbf{G}^{\alpha}) + \lambda_\alpha\mathbf{G}^{\beta}]\mathbf{p}^{\alpha} = 0 \text{ with } (\alpha,\beta) = (\{\mathrm{m},\mathrm{th}\},\{\mathrm{th},\mathrm{m}\}).$$

(+) Necessary conditions: $\varrho^{\mathrm{splr}}(\varrho_{\mathrm{cr}}) = \begin{cases}(1-\zeta)\varrho_{\mathrm{cr}} & \text{if } \varrho_{\mathrm{cr}} \le 1,\\ 1 & \text{if } \varrho_{\mathrm{cr}} > 1.\end{cases}$

(+) Sufficient conditions: $\varrho_{\mathrm{cr}} = \varrho_1 > 1$ with ϱ_{cr} is critical BLF of $\det(\mathbf{K} + \varrho\mathbf{G}^{\alpha}) = 0$.

- Automatically updates the penalty parameter until reaching the threshold

$$p^{(k+1)} = \min\{p, p^{(k)} + \max\{0, \Delta p^{(k)}\}\}$$

with the increment $\Delta p^{(k)} = \left[(1-\varsigma)\lambda^* - \lambda_{\mathrm{cr}}^{(k)} - \sum_{i,e}\left(\frac{\partial\lambda_{\mathrm{cr}}}{\partial\alpha_i^e}\right)^{(k)}(\Delta\alpha_i^e)^{(k)}\right] / \frac{\partial\lambda_{\mathrm{cr}}^{(k)}}{\partial p}.$

Numerical Examples

- Thermal Compliance Optimization of a 2D Column (proportional coupled buckling)

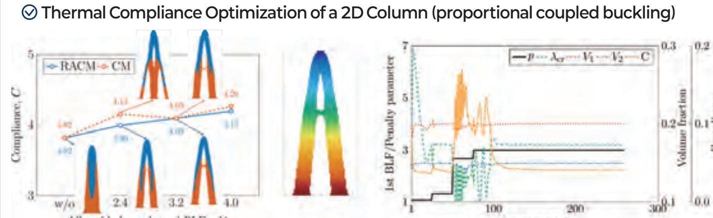

- p is adaptively updated, increasing only when λ_{cr} and C stabilize, thereby ensuring smoother convergence and more reliable topologies compared with the conventional continuum method (CM).

- Thermal Compliance Optimization of Curved Shell (decoupled buckling)

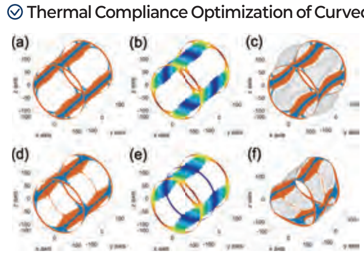

Optimized cylindrical with (α,β)=(m,th): (a-c) no BLF restriction, (d-f) critical BLF under λ^* =16.

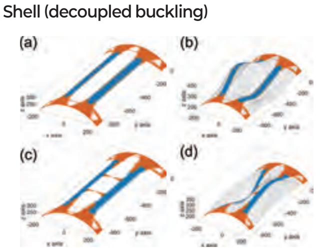

Optimized panel with (α,β)=(th,m): (a-b) no BLF restriction, (c-d) critical BLF under λ^* =2.

Acknowledgements & References

[1] Banh, T.T., Trinh, M.C. & Jun, H. (2025). Engineering with Computers, Revision submitted.
[2] Banh, T.T., Trinh, M.C. & Jun, H. (2025). Computer Methods in Applied Mechanics and Engineering, In revision.
[3] Trinh, M.C. & Jun, H. (2023). Thin-Walled Structures, 185: 110632.
[4] Jun, H. et al. (2018). Computer Methods in Applied Mechanics and Engineering, 337, 458-480.
[5] Trinh, M.C. & Jun, H. (2023). Engineering with Computers 39: 1459-97.

Medical AI

Application of Artifical Intelligent in ECG STEMI Diagnosis and Automatic Rodent Tracking for Clinical Experiments

Anh Tan Nguyen(응우옌탄안) [1], Minh-Chien Trinh(트린민췐) [2], Hyungmin Jun(전형민) [1,2,*]
School of Mechanical-Aerospace-Electric Convergence Engineering [1], Department of Mechanical Systems Engineering [2]
*hjun@jbnu.edu

Topic #1 GAN based Multi-resolution 12-lead ECG Reconstruction

Novel structure using GNN and CNN in a multi-resolution approach for accurately modelling the relationship between 12-lead ECG signals.

Encoder layers update the edge while decoder update nodes, constraining the reconstruction to the harnessed relationship between leads.

A novel Diffusion architecture that combines discrete wavelet transform and diffusion to reconstruct the signal in a multi-scale approach.

GAN Multi-resolution Network

GAN architecture

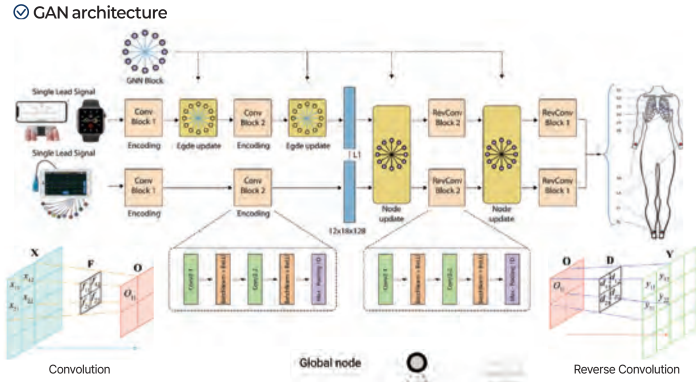

- Edge information encoding update

$$e_{uv}^{(l+1)} = \eta\left(x_u^{(l+1)}, x_v^{(l+1)}, e_{uv}^{(l)}\right)$$

- Node information decoding update

$$H^{(l+1)} = \sigma\left(D^{-\frac{1}{2}} A D^{-\frac{1}{2}} H^{(l)} W^{(l)}\right)$$

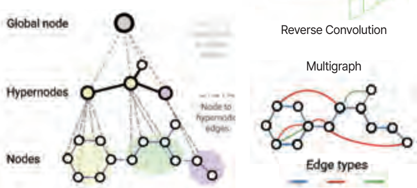

Energy based Multi-resolution Diffusion

Wavelet decomposition

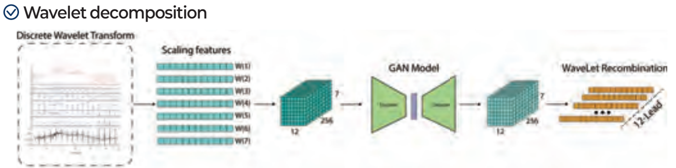

Wavelet filter reconstruction

$$\psi(x) := \sqrt{2}\sum_{k=0}^{2N-1}(-1)^k h_{2N-1-k}\varphi(2x-k)$$ follows

Energy condition: $$\sum_{k=0}^{N-1} h_{2k} = \frac{1}{\sqrt{2}} = \sum_{k=0}^{N-1} h_{2k+1}$$

Orthogonality: $$\sum_{k=0}^{2N-1+2l} h_k h_{2l+k} = \begin{cases}1, & \text{if } l = 0,\\ 0, & \text{if } l \neq 0\end{cases}$$

Filter matrix

$$a_k = (f, \varphi_k) = \int_R f(x)\varphi_k(x)\,dx$$

$$d_k = (f, \psi_k) = \int_R f(x)\psi_k(x)\,dx$$

Diffusion process

- Forward noise: $$q(\mathbf{x}_t \mid \mathbf{x}_{t-1}) = \mathcal{N}\left(\mathbf{x}_t; \sqrt{1-\beta_t}\mathbf{x}_{t-1}, \beta_t \mathbf{I}\right)$$ $$q(\mathbf{x}_{1:T} \mid \mathbf{x}_0) = \prod_{t=1}^{T} q(\mathbf{x}_t \mid \mathbf{x}_{t-1})$$
- Denoise: $$p_\theta(\mathbf{x}_{t-1} \mid \mathbf{x}_t) = \mathcal{N}\left(\mathbf{x}_{t-1}; \mu_\theta(\mathbf{x}_t, t), \sigma_t^2 \mathbf{I}\right)$$ Train params

Energy based noise diffusion

$$\nu_X^2(\tau_j) = \frac{\mathrm{var}\{X_j\}}{2^j} = \frac{\mathrm{var}\{X_j\}}{2\tau_j}$$

$$L_{\mathrm{simple}}(\theta) := \mathbb{E}_{t,\mathbf{x}_0,\epsilon}\left[\left\|\epsilon - \epsilon_\theta\left(\sqrt{\bar{\alpha}_t}\mathbf{x}_0 + \sqrt{1-\bar{\alpha}_t}\epsilon, t\right)\right\|^2\right]$$

Prediction sample

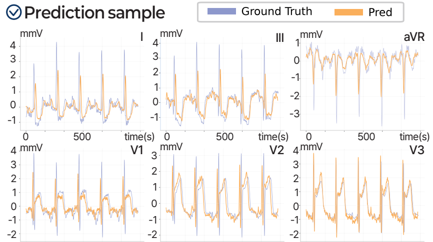

Benchmarks

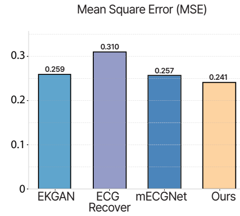

Topic #2 3D-CNNNet for Rodent Activity Tracking in Vaccination Effect Experiments

Novel structure using 3D CNN for direct spatial joint position prediction for rodents.

Application aimed at verifying vaccine effectiveness by performing statistical analysis of rodent pose estimation data collected over time from two experimental groups: a non-treatment control group and an MCAO treatment group.

3D Rodent Activity Experiments

Experiment setup

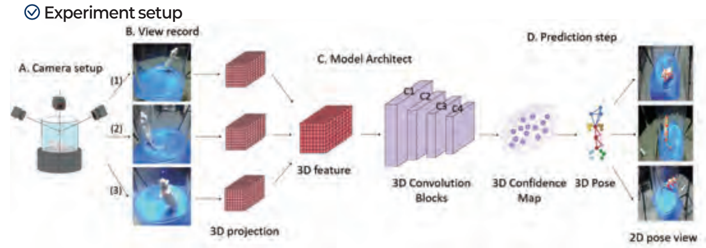

Camera calibration

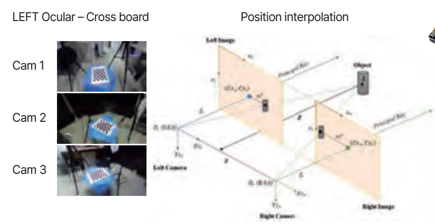

Binocular camera for depth estimation

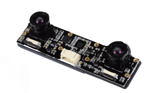

Enhance 3D interpolation accuracy

- Projection

$$s\begin{bmatrix}u\\v\\1\end{bmatrix} = \mathbf{K}[\mathbf{R}\ \ \mathbf{t}]\begin{bmatrix}X_w\\Y_w\\Z_w\\1\end{bmatrix}$$

- Minimize reprojection error

$$\min_{R,t}\sum_i\left\|\begin{bmatrix}u_i\\v_i\end{bmatrix} - \pi(K(R\mathbf{X}_w^i + t))\right\|^2$$

Analysis result

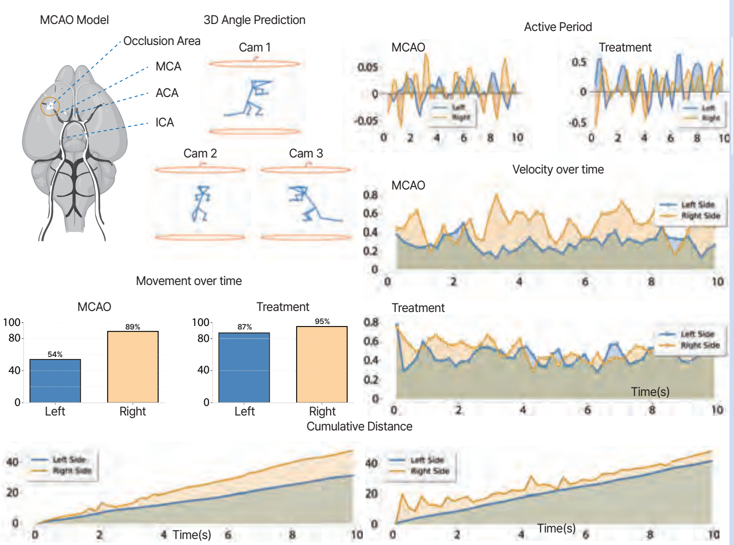

- MCAO group show **mid left-side impairment.**
- Treatment group show **balance improvement**

Acknowledgments & References

[1] Dunn, T.W., et al. (2021). Geometric deep learning enables 3D kinematic profiling across species and environments. Nature Methods, 18(5): 564–573.
[2] Percival, D. B. & Walden, A. T. (2000). Wavelet methods for time series analysis (Vol. 4). Cambridge university press.
[3] Nguyen, A.T., Trinh, M.C. & Jun, H. (2025). A Diffusion-based multi-resolution approach for reconstruction of 12-lead ECG from single lead in wearable devices, In preparation.

NRF 한국연구재단 KIAT iPET KHIDI 한국보건산업진흥원 BK21 FOUR

DNA Nanotechnology

DNA Automation Technology for Programmable Wireframe Origami and Higher-order Assemblies

Raja Muhammad Aqib(라자 무함마드아킵) [1], Minh-Chien Trinh(트린민췐) [1], Hyungmin Jun(전형민) [1,2,*]
Department of Mechanical Systems Engineering [1], School of Mechanical-Aerospace-Electric Convergence Engineering [2]
*hjun@jbnu.edu

Section #1 / DNA Automation Technology

DNA nanotechnology enables the construction of nanoscale structures with precise spatial control.

DNA automation tools streamline sequence generation, scaffold routing, and staple assignment, reducing manual design time from weeks to minutes.

Automated DNA design algorithms now make it possible to generate complex 2D and 3D wireframe architectures rapidly and reliably, accelerating research in molecular engineering, bio-nanofabrication, and programmable nanomaterials.

Automated Design Algorithms

General Overview of DNA Nanostructure Synthesis using Different Methodologies

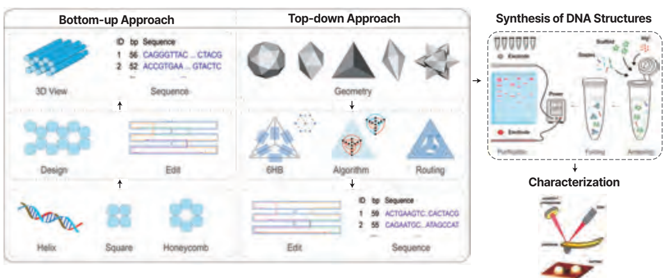

Geometry-Driven Designers

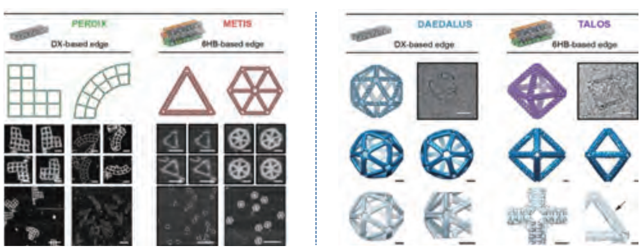

2D Wireframe DNA Origami

3D Wireframe DNA Origami

Design Software in DNA Nanotechnology

PERDIX (Programmed Eulerian Routing for DNA DesIgns using X-overs)

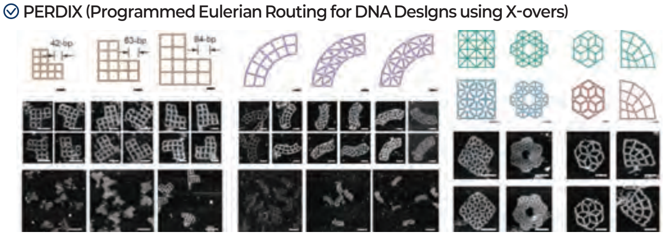

Variable Edge Length

Variable Vertex Degree

Variable Internal Meshes

METIS (Mechanically Enhanced and True orIgami Structures)

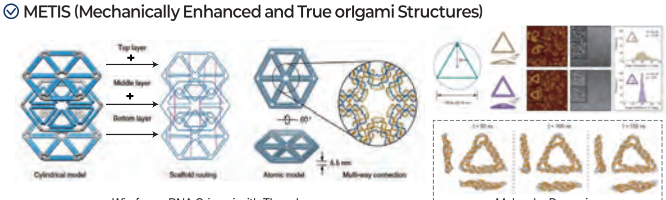

Wireframe DNA Origami with Three Layers

Molecular Dynamics

DAEDALUS

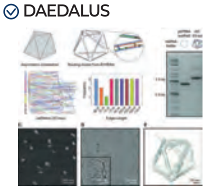

Controlled Arm Length (DX-edge Pairs)

TALOS

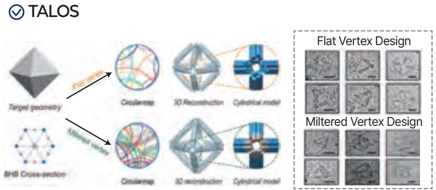

6-helix Bundles-edge Pairs

Section #2 / Modular Assembly with ATHENA

ATHENA provides an integrated platform to model, design, and generate sequences for wireframe DNA origami.

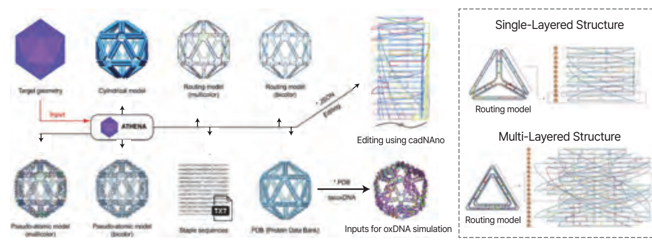

AuNP–DO Assembly

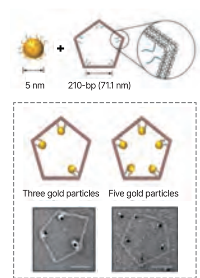

Supermolecular Assemblies

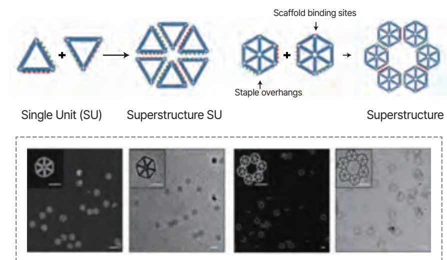

Self-limiting Finite Superstructures (Scale bars: 100 nm)

Higher-Order DNA Assemblies

ATHENA enables precise spatial patterning to create programmable nano-architectures, including higher-order DNA nanostructures.

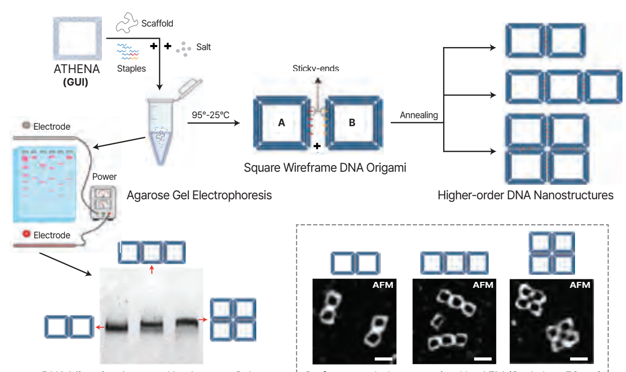

DNA Migration Assessed by Agarose Gel

Surface morphology examined by AFM (Scale bar: 50 nm)

Wireframe DNA origami was employed to construct programmable nanoscale alphabet structures.

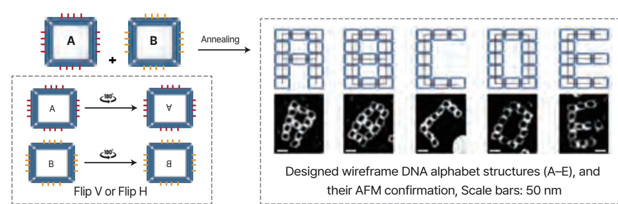

Designed wireframe DNA alphabet structures (A–E), and their AFM confirmation, Scale bars: 50 nm

Acknowledgments & References

[1] Aqib, R. M., Trinh, M.C. & Jun, H. (2026). In preparation.
[2] Trinh, M.C. & Jun, H. (2025). Advanced Materials Technologies: e00438.
[3] Wang, X., W., Li, S., Jun, H. et al. (2022). Science Advances, 8: eabn0039.
[4] Wang, X., Jun, H. & Bathe M. (2022). Journal of the American Chemical Society, 144(10): 4403–4409.
[5] Jun, H., et al. (2021). Nucleic Acids Research, 49(18): 10265-74.
[6] Jun, H., et al. (2019). Nature Communications, 10: 5419.
[7] Jun, H., et al. (2019). ACS Nano, 13(2), 2083–2093.
[8] Jun, H., et al. (2019). Science Advances, 5(1), eaav0655.